

1 **Impact of grids and dynamical cores in CESM2.2 on**
2 **the surface mass balance of the Greenland Ice Sheet**

3 **Adam R. Herrington¹, Peter H. Lauritzen¹, William H. Lipscomb¹, Marcus**
4 **Lofverstrom² and Andrew Gettelman¹**

5 ¹National Center for Atmospheric Research, 1850 Table Mesa Drive, Boulder, Colorado, USA

6 ²Department of Geosciences, University of Arizona, 1040 E. 4th Street, Tucson, AZ USA

7 **Key Points:**

- 8 • enter point 1 here
9 • enter point 2 here
10 • enter point 3 here

Abstract

[enter your Abstract here]

Plain Language Summary

[enter your Plain Language Summary here or delete this section]

1 Introduction

General Circulation Models (GCMs) are powerful tools for understanding the meteorology and climate of the high-latitudes, which are among the most sensitive regions on Earth to global and environmental change. Despite their importance, the numerical treatment of polar regions in GCMs is handled in vastly-different ways due to the so-called *pole-problem* (D. Williamson, 2007). The pole problem refers to numerical instability arising from the convergence of meridian lines into polar singularities on latitude-longitude grids (e.g., Figure 1a). Depending on the numerics, methods exist to suppress this instability, and latitude-longitude grids may be advantageous for polar processes as structures can be represented with more degrees of freedom than elsewhere in the computational domain. With the recent trend towards globally uniform unstructured grids, any potential benefits of latitude-longitude grids on polar regions may become a relic of the past. In this study a number of grids and dynamical cores (hereafter referred to as *dyccores*) available in the Community Earth System Model, version 2.2 (CESM2.2; Danabasoglu et al., 2020), including brand new variable-resolution grids, are evaluated to understand their impacts on the simulated characteristics of the Arctic, with a special focus on the climate and surface mass balance of the Greenland Ice Sheet.

In the 1970's the pole problem was largely defeated through wide-spread adoption of efficient spectral transform methods in GCMs. These methods transform grid point fields into a global, isotropic representation in wave space, where linear operators (e.g. horizontal derivatives) in the equation set can be solved for exactly. While spectral transform methods are still used in the 21st century, local numerical methods have become desirable for their ability to run efficiently on massively parallel systems. The pole problem has thus re-emerged in contemporary climate models that use latitude-longitude grids, and some combination of reduced grids and polar filters are necessary to ameliorate this instability (Jablonowski & Williamson, 2011). Polar filters are akin to a band-aid; they subdue the growth of unstable modes by applying additional damping to the solution over polar regions. This additional damping reduces the effective resolution in polar regions such that the resolved scales are approximately the same everywhere on the grid.

An alternative approach is to use unstructured grids, which allow for more flexible grid structures that permit quasi-uniform grid spacing globally and eliminates the pole-problem entirely (e.g., Figure 1c). This grid flexibility also permits variable-resolution or regional grid refinement (e.g., Figure 2). Grids can be developed with refinement over polar regions that could in principle make up for any loss in polar resolution in transitioning away from latitude-longitude grids (e.g., Figure 2), although this comes at the cost of a smaller CFL-limiting time-step in the refined region (the CFL-condition — short for Courant–Friedrichs–Lewy condition — is a necessary condition for numerical stability when using discrete data in time and space). Unstructured grids also scale more efficiently on parallel systems than latitude-longitude grids, likely resulting in a greater prevalence of unstructured grids as computing power continued to increase over time.

The meteorology and climate of the Arctic is characterized by a range of processes and scales that are difficult to represent in GCMs (Bromwich et al., 2001; Smirnova & Golubkin, 2017; van Kampenhout et al., 2018). For example, while synoptic scale storms are generally well represented at typical GCM resolutions of 1 to 2 degrees (Jablonowski

& Williamson, 2006; Stocker, 2014), mesoscale Polar Lows are not well resolved at these resolutions. These mesoscale systems are prevalent during the cold season and produce gale-force winds that can induce large heat and moisture fluxes through the underlying sea-ice/ocean interface. The Arctic also contains the Greenland Ice Sheet (hereafter denoted as *GrIS*). While it blankets the largest island in the world (Greenland), many of the processes that control the *GrIS* annual surface mass balance (the integrated sum of precipitation and runoff) are only partially resolved at typical GCM resolutions. For example, *GrIS* precipitation is concentrated at the ice-sheet margins, where orographic precipitation is generated by steep topographic slopes. *GrIS* ablation areas (marginal regions where seasonal melting exceeds the annual mass input from precipitation) are typically 10s to 100 km wide and confined to low-level areas or regions with limited precipitation. GCMs struggle to resolve the magnitude and extent of these features (Pollard, 2010; van Kampenhout et al., 2018), which can lead to unrealistic ice sheet growth in models with an interactive ice sheet component (e.g., Lofverstrom et al., 2020).

The goal of this study is to characterize the representation of high-latitude regions using the spectral-element and finite-volume dycores in CESM2.2, as these models treat the high-latitudes, e.g., the pole-problem, in different ways. The manuscript is laid out as follows: Section 2 consists of documentation of the grids, dycores and physical parameterizations used in this study. The Arctic refined grids were developed by the authors, and this section serves as their official documentation in CESM2.2. Section 2 also contains a description of the experiments along with the datasets and methods for evaluating the model simulations. Section 3 contains the results of the experiments, followed by Section 4 that provides a general discussion and conclusions.

2 Methods

2.1 Dynamical cores

The atmospheric component of CESM2.2, the Community Atmosphere Model, version 6.3 (CAM; Craig et al., 2021), supports a number of different atmospheric dynamical cores. These include dycores using latitude-longitude grids, such as finite-volume (FV; Lin, 2004) and eulerian spectral transform (EUL; Collins et al., 2006) models, and dycores built on unstructured grids, including spectral-element (SE; Lauritzen et al., 2018) and finite-volume 3 (FV3; Putman & Lin, 2007) models. The EUL dycore is the oldest dycore in CAM, and the least supported of all the dycores. FV3 is the newest dycore in CAM, but it was not fully incorporated at the time this work commenced; both the EUL and FV3 dycores are omitted from this study. As such, the results presented in this study are comparing the performance of the SE and FV dycores.

2.1.1 Finite-volume (FV) dynamical core

The FV dycore is a hydrostatic model that integrates the equations of motion using a finite-volume discretization on a spherical latitude-longitude grid (Lin & Rood, 1997). The 2D dynamics evolve in floating Lagrangian layers that are periodically mapped to Eulerian reference grid in the vertical (Lin, 2004), using a hybrid-pressure vertical coordinate. Hyperviscous damping is applied to the divergent modes while Laplacian damping is applied to momentum in the top few layers, referred to as a *sponge layer* (Lauritzen et al., 2011). A polar filter is used to avoid computational instability due to the convergence of the meridians, allowing for a more practical time-step. It takes the form of a Fourier filter in the zonal direction, with the damping coefficients increasing monotonically in the poleward direction (Suarez & Takacs, 1995).

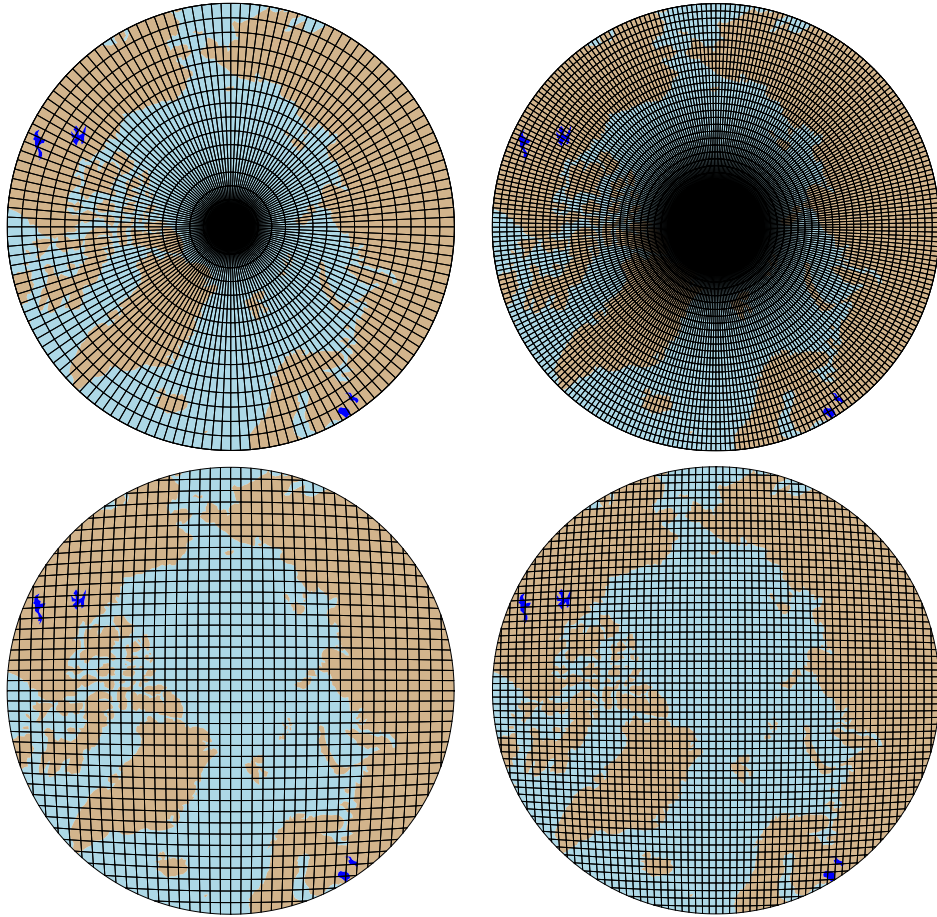


Figure 1. Computational grids for the uniform $1^\circ - 2^\circ$ grids in this study.

105 **2.1.2 Spectral-element (SE) dynamical core**

106 The SE dycore is a hydrostatic model that integrates the equations of motion us-
 107 ing a high-order continuous Galerkin method (Taylor et al., 1997; Taylor & Fournier, 2010).
 108 The computational domain is a cubed-sphere grid tiled with quadrilateral elements (e.g.,
 109 Figure 2). Each element contains a fourth order basis set in each horizontal direction,
 110 with the solution defined at the roots of the basis functions, the Gauss-Lobatto-Legendre
 111 (GLL) quadrature points. This results in 16 GLL nodal points within each element, with
 112 12 of the points lying on the (shared) element boundary. Communication between el-
 113 ements happens via the direct stiffness summation (Canuto et al., 2007), which applies
 114 a numerical flux to the element boundaries that reconciles overlapping nodal values and
 115 produces a continuous global basis set.

116 As with the FV dycore, the dynamics evolve in floating Lagrangian layers that are
 117 subsequently mapped to an Eulerian reference grid. A dry mass vertical coordinate was
 118 more recently implemented for thermodynamic consistency with condensates (Lauritzen
 119 et al., 2018). The 2D dynamics have no implicit dissipation and so hyperviscosity op-
 120 erators are applied to all prognostic variables to remove spurious numerical errors (Dennis
 121 et al., 2012). Laplacian damping is applied in the sponge layer.

122 The SE dycore supports regional grid refinement via its variable-resolution config-
 123 uration, requiring two enhancements over uniform resolution grids. (1) As the numer-



Figure 2. Spectral-element grid for the variable-resolution ARCTIC grid in this study. Note that this is not the computational grid; each element has 3×3 independent grid points.

ical viscosity increases with resolution, explicit hyperviscosity relaxes according to the local element size, reducing in strength by an order of magnitude per halving of the grid spacing. A tensor-hyperviscosity formulation is used (Guba et al., 2014), which adjusts the coefficients in two orthogonal directions to more accurately target highly distorted quadrilateral elements. (2) The topography boundary conditions need to be smoothed in a way that does not excite grid scale modes, and so the NCAR topography software (Lauritzen et al., 2015) has been modified to scale the smoothing radius by the local element size.

For spectral-element grids with quasi-uniform grid spacing, a variant in which tracer advection is computed using the Conservative Semi-Lagrangian Multi-tracer transport scheme (CSLAM) is used instead (Lauritzen et al., 2017). CSLAM has improved tracer property preservation and accelerated multi-tracer transport. It uses a separate grid from the spectral-element dynamics, through dividing each element into 3×3 control volumes with quasi-equal area. The physical parameterizations are computed from the state on the CSLAM grid, which has clear advantages over the default SE dycore in which the physics are evaluated at the GLL nodal points (A. Herrington et al., 2018).

2.2 Grids

Six grid are evaluated in this study (Table 1). The FV dycore is run with 1° and 2° grid spacing, referred to as $f09$ and $f19$, respectively (Figure 1a,b). The 1° equivalent of the CAM-SE-CSLAM grid is also run, referred to as $ne30pg3$ (Figure 1c), where ne refers to a grid with of $ne \times ne$ elements per cubed-sphere face, and pg denotes that there are $pg \times pg$ control volumes per element for computing the physics. An additional 1° CAM-SE-CSLAM grid is run, but with the physical parameterizations computed on a grid that contains 2×2 control volumes per element, $ne30pg2$ (Figure 1d; A. R. Herrington et al., 2019).

Two variable resolution meshes were developed as part of the CESM2.2 release that contains grid refinement over the Arctic (Figure 2). This manuscript serves as the official documentation of these grids. The Arctic meshes were developed using the software package SQuadgen (<https://github.com/ClimateGlobalChange/squadgen>). The ARCTIC grid is a 1° grid with $\frac{1}{4}^\circ$ regional refinement over the broader Arctic region.

grid name	dycore	Δx_{eq} (km)	Δx_{refine} (km)	Δt_{phys} (s)
<i>f19</i>	FV	278	-	1800
<i>f09</i>	FV	139	-	1800
<i>ne30pg2</i>	SE-CSLAM	167	-	1800
<i>ne30pg3</i>	SE-CSLAM	111	-	1800
<i>ne30pg3*</i>	SE-CSLAM	111	-	450
<i>ARCTIC</i>	SE	111	28	450
<i>ARCTICGRIS</i>	SE	111	14	225

Table 1. Grids and dycores used in this study. Δx_{eq} refers to average equatorial grid spacing, Δx_{refine} refers to grid spacing in the refined region (if applicable) and Δt_{phys} refers to the physics time-step. The dycore abbreviation FV refers to the finite-volume dycore, SE the spectral-element dycore and SE-CSLAM the spectral-element dycore w/ CSLAM tracer advection.

154 The *ARCTICGRIS* grid is identical to the *ARCTIC* grid, but contains an additional
 155 patch covering the big island of Greenland with $\frac{1}{8}^{\circ}$ resolution.

156 The physics time-step should depend on grid resolution. Increases in horizontal res-
 157 olution permit faster vertical velocities that reduce characteristic time-scales, and so the
 158 physics time-step is reduced to avoid large time truncation errors (A. Herrington & Reed,
 159 2018). The *ARCTIC* and *ARCTICGRIS* grids are run with a 4× and 8× reduction
 160 in physics time-step relative to the default 1800 s time-step used in the standard 1°–
 161 2° grids (Table 1).

162 All grids and dycores in this study use 32 levels in the vertical, with a model top
 163 of about 1 hPa or about 40 km. However, any grid or dycore can in principle be run with
 164 a higher-top and/or with finer vertical resolution.

165 2.3 Physical parameterizations

166 The CAM6.3 physical parameterization package (hereafter referred to as the *physics*;
 167 Craig et al., 2021) is used in all simulations in this study. CAM version 6 physics and
 168 later is most notably different from its predecessors through the incorporation of high-
 169 order turbulence closure, Cloud Layers Unified by Binormals (CLUBB; Golaz et al., 2002;
 170 Bogenschutz et al., 2013), which jointly acts as a PBL, shallow convection and cloud macro-
 171 physics scheme. CLUBB is coupled with the MG2 microphysics scheme (Gettelman et
 172 al., 2015), with prognostic precipitation and classical nucleation theory in representing
 173 cloud ice for improved cloud-aerosol interactions. Deep convection is parameterized us-
 174 ing a convective quasi-equilibrium, bulk plume mass flux scheme (Zhang & McFarlane,
 175 1995; Neale et al., 2008) and includes convective momentum transport (Richter et al.,
 176 2010). PBL form drag is modeled after (Beljaars et al., 2004) and orographic gravity wave
 177 drag is represented with an anisotropic method informed by the orientation of topographic
 178 ridges at the sub-grid scale.

179 Initial simulations with the *ne30pg3* spectral-element grid produced weaker short-
 180 wave cloud forcing relative to the tuned up finite-volume dycore. All runs with the spectral-
 181 element dycore have two CLUBB parameter changes in order to provide a more realis-
 182 tic cloud forcing and top-of-atmosphere radiation balance. These are CLUBB’s *gamma*
 183 parameter, reduced from 0.308 to 0.270, and *c14*, reduced from 2.2 to 1.6. Briefly, the
 184 *gamma* parameter scales the width of the sub-grid distribution of vertical velocity, and
 185 *c14* controls the strength of the damping term in the equation for the horizontal com-
 186 ponent of turbulent kinetic energy. For a thorough explanation of how CLUBB param-
 187 eters impact the simulated climate, the reader is referred to (Guo et al., 2015).

188 **2.4 Experimental design**

189 All grids and dycores are run using an identical transient 1979-1998 AMIP-style
 190 configuration, with prescribed monthly SST/sea-ice after (Hurrell et al., 2008). This con-
 191 figuration refers to the *FHIST compset* and runs out of the box in CESM2.2.

192 The surface mass balance (SMB) of the Greenland Ice Sheet (GrIS) is simulated
 193 in all grids and dycores in this study. The SMB is the sum of the mass source term, ac-
 194 cumulation (i.e., precipitation), and the mass sink term, ablation. Ablation can be ex-
 195 pressed as evaporation/sublimation plus total runoff, with runoff being a combination
 196 of liquid precipitation and snow and ice melt. Not all liquid precipitation becomes runs
 197 off the ice sheet; rain may penetrate pore spaces in the firn layer and freeze, forming ice
 198 lenses in the subsurface. These processes are represented by different components in CESM,
 199 but it is the Community Land Model, version 5 (CLM; Lawrence et al., 2019), that ag-
 200 ggregates these processes and computes the SMB.

201 CLM runs on the same grid as the atmosphere, but also uses a downscaling tech-
 202 nique to account for sub-grid variability in SMB. In short, the ice sheet patch in a CLM
 203 grid cell is subdivided into 10 elevation classes (EC), weighted by their respective area
 204 fractions at each EC, which is derived from a high resolution GrIS elevation dataset. The
 205 near surface air temperature, humidity and air density are calculated at each EC using
 206 an assumed lapse rate and the elevation difference from the grid mean, and the precip-
 207 itation rates from CAM are repartitioned into solid or liquid based on the temperature
 208 of the EC. Ice accumulation is modeled as a capping flux, or snow in excess of a 10 m
 209 snow cap, and refreezing of liquid within the snowpack additionally acts as a source of
 210 ice. A unique surface energy balance and SMB is computed for each EC. Integrating over
 211 all ECs using the area weights provides a more accurate SMB. For a more detailed de-
 212 scription of how the SMB is computed in CESM, the reader is referred to (Lipscomb et
 213 al., 2013; Sellevold et al., 2019; van Kampenhout et al., 2020).

214 Since the 10 m snowcap needs to be reached in the accumulation zone to simulate
 215 the SMB, the snow depths in the variable-resolution grids were spun-up by forcing CLM
 216 in standalone mode, cycling over a 20 year *ARCTIC FHIST* run for about 500 years.
 217 The uniform resolution grids are all initialized with an SMB from an existing *f09* spun-
 218 up initial condition.

219 **2.5 Observational Datasets**

220 Several observational datasets are used in this study to understand the performance
 221 of the simulations. A list of the datasets used in this study are shown in Table 2. Sev-
 222 eral of these products (ERA5, CALIPSO and CERES) are near-global gridded datasets
 223 commonly used to evaluate GCMs. Surface mass balance datasets were initially gath-
 224 ered from several sources. RACMO2.3 11km and RACMO2.3p2 5.5km are regional model
 225 simulations targeting Greenland, forced by ERA interim and ERA5 renalyses at its do-
 226 main boundaries. The RACMO simulations have been shown to performs very skillfully
 227 against observations and is therefore considered an ideal modeling target (Noël et al.,
 228 2015, 2019).

229 In-situ SMB (snow pit and ice cores) and radar accumulation datasets (e.g., Ice-
 230 Bridge) are conveniently maintained in The Land Ice Verification and Validation toolkit
 231 (LIVVkit), version 2.1 (Evans et al., 2019). However, these point-wise measurements are
 232 difficult to compare to model output spanning several different grids, and would be more
 233 useful if the surface mass balance from the individual EC's were available from the model
 234 output, which they are not. A nearest neighbor technique was used to do an initial anal-
 235 ysis, and indicated that the model biases are similar to those computed using the RACMO
 236 datasets. Owing to the uncertainty of comparing gridded fields to point-wise measure-

data product	years used in this study	resolution	citation
ERA5	1979-1998	$\frac{1}{4}^\circ$	Copernicus (2019)
CERES-EBAF ED4.1	2003-2020	$\frac{1}{4}^\circ$	Loeb et al. (2018)
CALIPSO-GOCCP	2006-2017	1°	Chepfer et al. (2010)
RACMO2.3	1979-1998	11 km	Noël et al. (2015)
RACMO2.3p2	1979-1998	5.5 km	Noël et al. (2019)

Table 2. Description of observational datasets used in this study.

ments, and the lack of additional information it adds with regard to model biases, these datasets were omitted from the analysis in this study.

2.6 SMB Analysis

A common high resolution dataset is used to generate the GrIS boundary conditions in all grids, using the CLM dataset creation tools. Since we are interested in the total ice sheet SMB, we seek to integrate various components of the SMB over a common ice mask to get the total mass change of the GrIS. Figure 3 shows the GrIS ice mask area errors (computed as percent differences from the high resolution dataset) across the different grids, and as a function of the number of grid points. Due to the use conservative regridding in the CLM tools, the interpolation errors are small and ice mask areas have less than 1.5% errors relative to the raw ice mask dataset. RACMO2.3, however, uses a smaller ice mask, about 3% smaller than the raw ice mask dataset.

The area errors in Figure 3 don't seem large, but even small changes in ice mask area can lead to large differences in integrated SMB (Hansen et al., 2022). Therefore, we have taken the approach of mapping all model fields to the lowest resolution grids and integrating over the respective low resolution ice masks. Due to the sensitivity of mapping errors to grid coordinates (i.e., unstructured or structured), all quantities are evaluated on both the *f19* and *ne30pg2* grids, the lowest resolution grid for each dycore considered in this study. In addition, two remapping algorithms are used; Earth System Modeling Framework (ESMF; Team et al., 2021) first-order conservative and TempestRemap (Ullrich & Taylor, 2015) high-order, monotone algorithm. In all, each integrated quantity is evaluated (at most) four times to provide an estimate of uncertainty due to differences in grid coordinates and remapping algorithm.

3 Results

3.1 Tropospheric temperatures

Before delving into the simulated characteristics of the Arctic, the global mean differences between the various grids and dycores are assessed. Figure 4 shows 1979-1998 annual mean, zonal mean height plots expressed as differences between the uniform resolution grids and dycores. The *f09* grid is warmer than the *f19* grid, primarily in the mid-to-high latitudes and throughout the depth of the troposphere. This is a common response to increasing horizontal resolution in GCMs (Pope & Stratton, 2002; Roeckner et al., 2006), and A. R. Herrington and Reed (2020) has shown that this occurs in CAM due to greater resolved vertical velocities that in turn, facilitate greater condensational heating in the macrophyiscs routine in CLUBB. The right columns in Figure 4 supports this interpretation, which shows an increase in the climatological CLUBB heating in the low and mid-latitudes in the *f09* grid.

As the SE dycore is less diffusive than the FV dycore, the resolved vertical velocities are larger in the SE dycore, and so a modest, resolution-like sensitivity occurs in which *ne30pg3* is warmer than *f09* (Figure 4). The stratosphere has a uniquely differ-

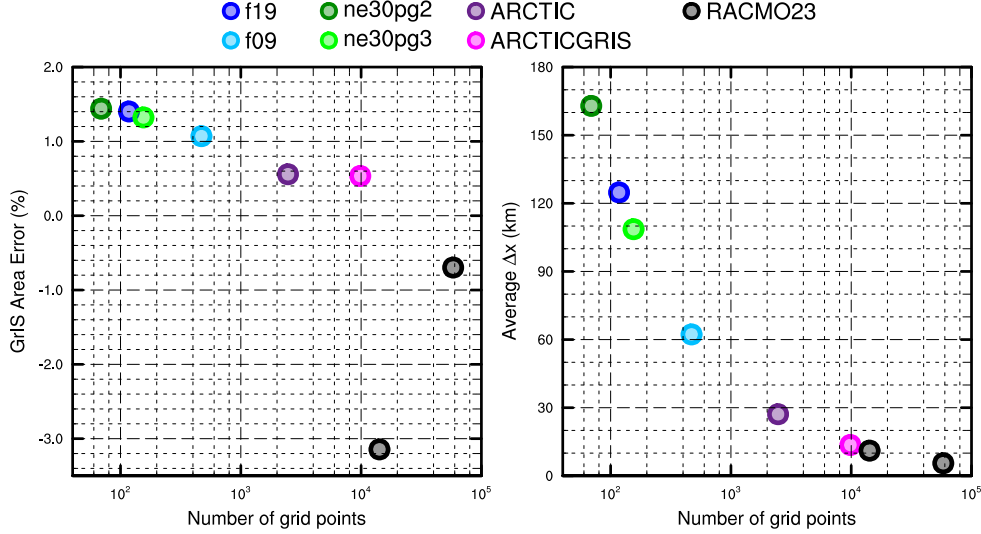


Figure 3. The spatial properties of the GrIS as represented by different grids in this study. (Left) GrIS area error, computed as the relative differences from a 4km dataset used to create the CESM ice masks, (right) approximate average grid spacing over GrIS.

ent response, in which *ne30pg3* is much cooler than *f09* in the mid-to-high latitudes. Figure 4 also shows differences in temperature between *ne30pg3* and *ne30pg2*, which are small, although there is a slight warming near the tropopause at high latitudes. This is consistent with the similar climates found between these grids in A. R. Herrington et al. (2019).

Comparing the variable-resolution grids to the uniform resolution grids is complicated because we simultaneously increase the grid resolution and reduce the physics time-step, both of which noticeably impact the solution (D. L. Williamson, 2008). An additional *ne30pg3* simulation is run with the physics time-step used in the *ARCTIC* grid, referred to as *ne30pg3**. Figure 5 shows the change in the climatological summer temperatures in zonal-mean height space between *ne30pg3** and *ne30pg3*. A similar warming response to increasing resolution occurs when the time-step is reduced, and the mechanism is similar in that the shorter time-step facilitates greater condensational heating by CLUBB. Figure 5 shows the difference in climatological summer temperature between the *ARCTIC* grid and the *ne30pg3** grid. The greater condensational heating and warmer temperatures are confined to the regionally refined region when the impact of physics time-steps is removed from the comparison.

Figure 5 indicates that the *ARCTICGRIS* grid is a lot warmer than the *ARCTIC* grid in the Arctic. Part of this may be due to the shorter physics time-step; a similar physics-time-step sensitivity in the *ne30pg3** comparison is evident in the CLUBB tendencies in the *ARCTICGRIS* grid. However, the temperature response is disproportionately large relative to the change in CLUBB tendencies. This summer warming appears to be a result of variations in the stationary wave pattern, with anomalous southerly winds occurring to the west of Greenland (not shown). This dynamic response is extremely interesting because other than the physics time-step, the only difference between *ARCTICGRIS* and the *ARCTIC* grid is the doubling of resolution of Greenland. This behavior will be explored more fully in a future study.

It's useful to understand summer temperature biases due to its control on ice/snow melt over the Greenland Ice Sheet (GrIS; Ohmura, 2001). Figure 6 shows the 1979-1998

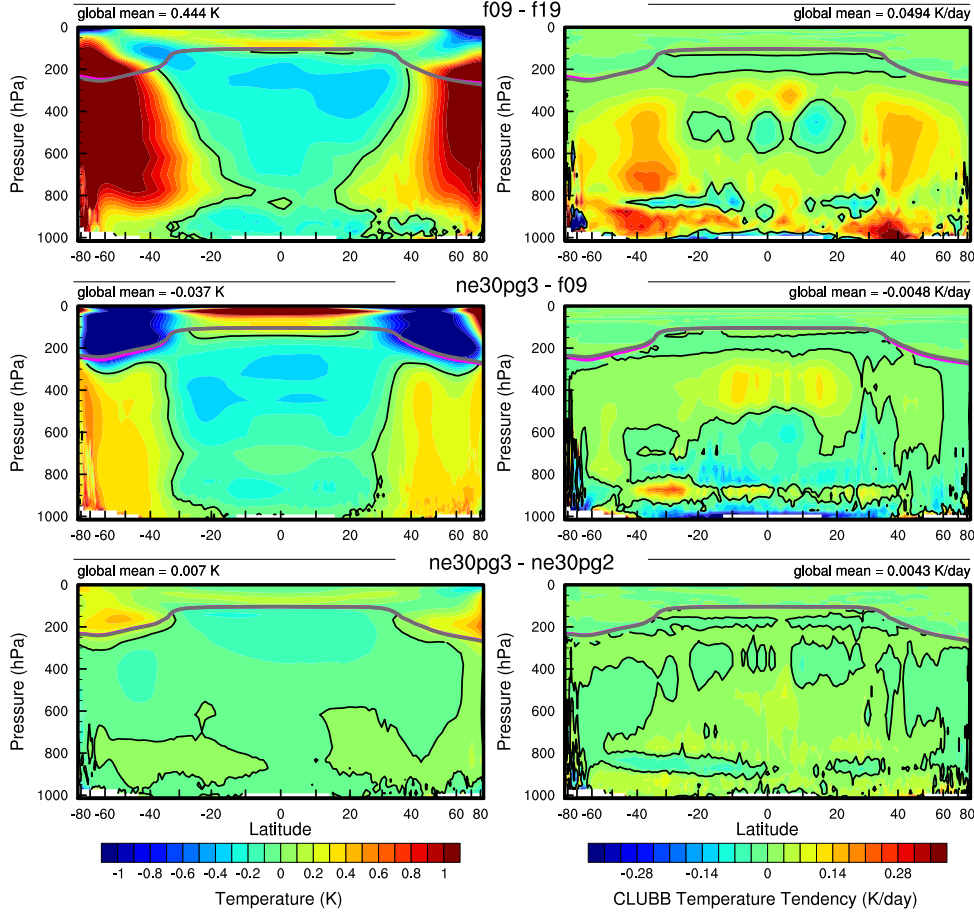


Figure 4. 1979–1998 annual mean (left column) temperature and (right column) CLUBB temperature tendencies in zonal mean height space, expressed as differences between the various 1° – 1° grids. The thick grey and magenta lines are the tropopause for control run and the test run, respectively.

lower troposphere summer temperature bias relative to ERA5. It is computed from the 500 hPa–1000 hPa geopotential thickness, solving for the layer mean virtual temperature using the hypsometric equation. The results generally track with the analysis of the zonal mean height plots; increasing resolution from *f19* to *f09* leads to a warmer climate, and the 1° spectral-elements grids are warmer than the finite-volume grids. The summer temperatures in the finite-volume grids are persistently colder than ERA5, whereas the 1° spectral-element grids are not as cold, and are actually warmer than ERA5 at very high-latitudes, north of 75° . All grids illustrate a north-south gradient in bias over Greenland, in which the summer temperature bias becomes more positive on the northern side of the ice sheet. This pattern is also evident in the 2m summer temperature bias over Greenland (not shown).

The *ARCTIC* grid has similar summer temperatures to the 1° spectral-element grids, but it is a bit warmer over northern Eurasia and the North Pole. An anomalous cooling patch forms to the west of Greenland, centered over Baffin Island. The *ARCTICGRIS* grid is warmer than the *ARCTIC* grid over most of the Arctic, but maintains a similar spatail pattern of summer temperature bias as in the *ARCTIC* grid.

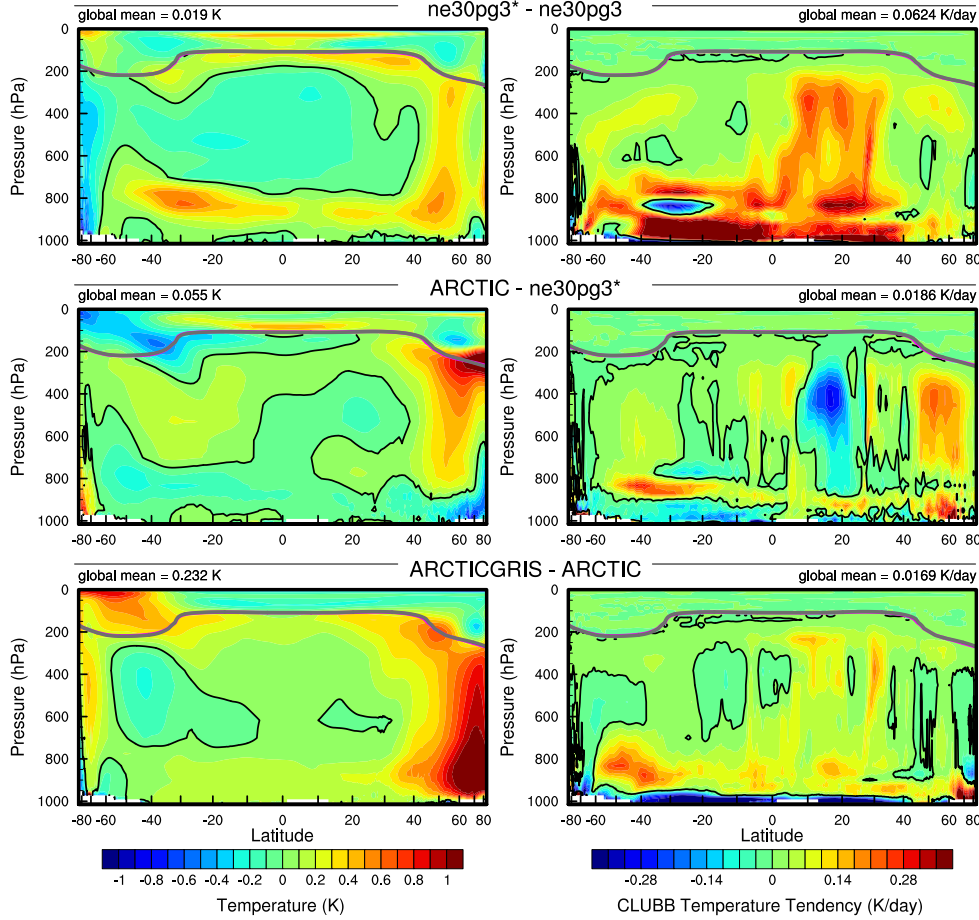


Figure 5. As in Figure 4 but for the short-time step experiment and the variable-resolution grids. The fields plotted are for the climatological northern hemisphere summer. The focus on summer is because that is when the resolution response is largest, and the refined regions are located in the northern hemisphere.

Some of these temperature anomalies may be related to summer shortwave cloud forcing differences across the different grids and dycores. Figure 7 shows the summer shortwave cloud forcing bias in the runs, using the CERES-EBAF product. All the uniform 1° – 2° grids have similar biases, with the clouds reflecting 20–40 W/m² too much shortwave radiation over a wide swath of the Arctic, primarily over the land masses. There's also a halo of low cloud forcing bias around the oceanic perimeter of Greenland. The *ARCTIC* grid has much smaller cloud forcing biases over the Arctic land masses, although still too reflective, whereas the *ARCTICGRIS* grid vastly improves the cloud forcing bias over Eurasia, and improves the bias over N.America compared to the *ARCTIC* grid. In both variable-resolution grids, the halo of too weak cloud forcing bias around the perimeter of Greenland is absent.

While the summer cloud forcing biases are consistent with the summer temperature biases in Figure 6 –regions where clouds are too reflective coincide with regions that are too cold– it is not clear whether the cold biases are caused by the cloud biases, or whether the cold biases amplify the cloud forcing bias.

335 3.2 Shortwave radiation over Greenland

336 In addition to summer temperatures, shortwave radiation is also an important de-
 337 terminant of snow/ice melt. Figure 8 shows the summer incident shortwave radiation
 338 bias at the surface, zoomed in over Greenland. The top panel computes the bias using
 339 the CERES-EBAF dataset, and the bottom panel using RACMO2.3p2 dataset. This halo
 340 of excessive incident shortwave radiation around the coasts of Greenland is apparent in
 341 both datasets, consistent with the shortwave cloud forcing biases in Figure 7.

342 The interior of the ice sheet receives too little shortwave radiation in the coarser
 343 grids. In the variable-resolution grids, both the interior deficit in shortwave and the ex-
 344 cessive shortwave around the oceanic perimeter of Greenland are improved. This sug-
 345 gests that the coarse grids clouds are too thick in the interior of Greenland, and too thin
 346 around the perimeter of Greenland, and that increasing horizontal resolution balances
 347 out these biases. This is consistent with total summer cloud fraction bias, computed from
 348 the CALIPSO-GOCCP cloud dataset (Figure 9). Note that total cloud fraction char-
 349 acterizes the cloud field at all vertical levels, but attenuates any changes arising from any
 350 single layer due to the maximum overlap assumption used to compute this quantity. De-
 351 spite the attenuated signal, the total cloud fraction does indicate a reduction in cloud
 352 coverage in the interior, and an increase in cloudiness about the oceanic perimeter, in
 353 the variable-resolution grids.

354 The agreement of the cloud biases in and around Greenland from multiple inde-
 355 pendent datasets indicates this is a robust feature of the coarser grids. The reduction
 356 of these cloud biases in the variable-resolution grids suggests they are a result of insuf-
 357 ficient horizontal resolution in the coarse grids.

358 3.3 Greenland surface mass balance

359 The accuracy of the simulated SMB is expected to be sensitive to grid resolution.
 360 Figure 9 shows the average grid spacing over the Greenland Ice Sheet (GrIS) in all six
 361 grids in this study. The *ne30pg2* grid has the coarsest representation with an average
 362 $\Delta x = 160 \text{ km}$, and the *ARCTICGRIS* grid has the highest resolution with an aver-
 363 age $\Delta x = 14.6 \text{ km}$, similar to the grid spacing of the 11 km RACMO2.3 grid. The *ne30pg3*
 364 grid has an average $\Delta x = 111.2 \text{ km}$, which is substantially more coarse than the *f09*
 365 grid, with an average $\Delta x = 60 \text{ km}$. This is interesting because *ne30pg3* and *f09* have
 366 similar average grid spacing over the entire globe, and comparable computational costs,
 367 but due to the convergence of meridians the finite-volume model has enhanced resolu-
 368 tion over GrIS. The *ARCTIC* grid has an average grid spacing of $\Delta x = 27.8 \text{ km}$, and
 369 is about 10 times more expensive than the 1° models (whereas the *ARCTICGRIS* grid
 370 is about twice as expensive as the *ARCTIC* grid).

371 The summer climatological mean precipitation bias over GrIS is shown in Figure 3,
 372 expressed as the fractional difference from the RACMO2.3p2 solution. What sticks out
 373 is that the coarse $1^\circ - 2^\circ$ grids have large, positive biases centered over the southern
 374 dome. The *ARCTIC* run improves this bias substantially, and the *ARCTICGRIS* run
 375 improves this bias further. This suggests the southern dome bias is due to inadequate
 376 horizontal resolution, which is consistent with the original GrIS variable-resolution ex-
 377 periments in (van Kampenhout et al., 2018).

378 Southeast Greenland has the largest accumulation rates in GrIS due to synoptic
 379 systems moving in from the southeast. These systems are orographically lifted by the
 380 steep southeast ice sheet margin, dumping large amounts of precipitation along the south-
 381 east coast. At lower horizontal resolutions, the topography is too smooth and large amounts
 382 of moisture penetrates further inland, incorrectly dumping precipitation onto the inte-
 383 rior of the ice sheet. A similar bias occurs in northwest Greenland, in particular during
 384 the summer, when it's common for synoptic systems to arrive from the southwest. The

ability of the variable-resolution grids to more accurately simulate the orographic precipitation process in Greenland is consistent with all the cloud results up to this point. Since the precipitation centers move from the interior towards the coasts, and even out over the ocean with increasing resolution, the cloud decks should, and are, moved accordingly, eliminating this halo of low cloud bias around the oceanic perimeter of Greenland.

Figure 10 shows time-series of annually integrated precipitation and snow/ice melt over the GrIS in the various different grids and dycores, with both versions of RACMO shown in black. The 1979-1998 climatological mean values are provided as circles on the right side of the panels. The uniform $1^{\circ} - 2^{\circ}$ grids all show a distinctive positive bias in precipitation due to this over-prediction of interior precipitation rates. The variable-resolution grids have the smallest precipitation biases, providing a comparable solution to RACMO. The *f19* and *f09* perform similarly, with +110 Gt/yr bias, whereas *ne30pg3* is biased by about +165 Gt/yr and *ne30pg2*, +230 Gt/yr. The results suggest that uniform resolution spectral-element grids have larger biases than the finite-volume grids, consistent with spectral-element grids having a coarser representation of GrIS (Figure 3).

The combined annual snow/ice melt integrated over the GrIS is shown in the bottom panel of Figure 10. The *ARCTIC* grid simulates the most realistic melt rates, with all other grids tending to have larger melt rates than RACMO. The *ARCTICGRIS* grid over predicts melting by about 125 Gt/yr. This is likely due to an anomalously warm lower troposphere during the summer, relative to the *ARCTIC* run (Figure 6). The *f19* and *f09* melting rates are improved over *ARCTICGRIS*, overestimating melt by only 70-90 Gt/yr. The spectral-element grids have the largest positive melt bias, between 200-220 Gt/yr. It is more difficult to attribute these differences to resolution alone, since the finite-volumes grids have colder summer temperatures than the uniform resolution spectral-element grids. However, that the *ARCTCIGRIS* grid has the warmest summer temperatures, yet has a lower melting bias than the uniform spectral-element grids, suggests that increasing resolution improves the ablation process.

To get an idea of the regional behavior of the SMB components, Figure 11 shows the precipitation and combined snow/ice melt integrated over the basins defined by (Rignot & Mouginot, 2012). The uncertainty due to differences in basin area is larger than for GrIS wide integrals, owing to the differences in basin boundaries as represented on the *f09* and *ne30pg2* grids (Figure 12), which pertains to the grids in which all integrals are evaluated. Nonetheless, the southeast and southwest basins have the largest accumulation totals. All the basins exhibit a monotonic reduction of accumulation rates with increasing grid resolution, with some exceptions. The *ARCTCIGRIS* grid simulates less precipitation than RACMO in the central-east and southeast basins. Conversely, the *ARCTCIGIS* precipitation is closest to the RACMO value in the large southwest basin.

The basin integrated melt rates in Figure 11 show a different grid sensitivity than the precipitation rates. Of note is that the uniform-resolution spectral-element grids have the largest positive bias in melt rates, in all basins, with the *ARCTICGRIS* grid a close second. This is somewhat unexpected as the *ARCTCIGRIS* grid has the warmest lower troposphere summer temperatures (Figure 6) and incident shortwave radiation (Figure 6), yet it has less melting than the uniform-resolution spectral element grids. Lower troposphere temperature is not a strict proxy for melting; e.g., it may not capture local elevation effects as a result of a better representation of the low-elevation ablation zones. A more accurate proxy for the impact of temperature on melting is positive degree days (PDD; Braithwaite, 1984). PDD is a metric that accumulates the near surface temperature in C° for any day in which the temperature is above freezing. PDD is non-linear in mean monthly near surface temperature (Reeh, 1991), and we compute it using monthly means 2-meter temperature using the method of Calov and Greve (2005).

The basin integrated PDD melt estimate is shown in Figure 11. One interesting feature is that in the big southeast and southwest basin (and all the other western basins),

grid name	accumulation (Gt/yr)	ice/snow melt (Gt/yr)
<i>RACMO</i>	768.5	-347.2
<i>f19</i>	882.5	-440.3
<i>f09</i>	874.8	-418.4
<i>ne30pg2</i>	1000.	-549.4
<i>ne30pg3</i>	934.9	-568.8
<i>ARCTIC</i>	795.9	-367.3
<i>ARCTICGRIS</i>	708.7	-471.6

Table 3. 1979-1998 Surface Mass Balance of the Greenland Ice Sheet.

the *ne30pg3* grid has larger PDD based melt than the *ARCTICGRIS* grid. The southwest basin also predicts a rather large PDD based melt in the finite-volume grids, relative to the *ARCTICGRIS* grid. The PDD plots indicate that the near surface temperatures expected to contribute to melt is not well approximated by the summer lower troposphere temperatures in Figure 6.

Figure 12 shows the biases in the combined ice/snow melt as map plots. This plot is quite revealing as it indicates that the largest melt biases occur on the southeast and northwest coast, where large coarse grid cells overlap with the ocean. One possibility is that these problematic grid cells are situated at lower elevations then the ice sheet surface exists in nature, leading to too warm of a state and overestimating the melt. Figure 13 shows the representation of the surface of the ice sheet along two transects in the different grids, compared to the high resolution dataset used to generate CAM topography boundary conditions (GMTED). The two transects are shown in Figure 12; the infamous "k-transect" in southwest Greenland and a transect extending from the central dome down to the highly productive Kangerlussuaq glacier on the southeast coast. The 1° – 2° grids are noticeably coarse, with only a handful of grid cells populating the transect. The *f09* grid is a bit of an exception; the grid cells become very narrow in the meridional direction at high latitudes, a larger number of grid cells can populate the east-west transect. The variable-resolution grids are more skillful at reproducing the steep margins of the ice sheet, capturing the parabolic shape of ice sheets.

While the two transects in Figure 13 only two anecdotes, they indicate that the ice sheet surface is not systematically lower than the true surface in the coarse grids, near the ice margins. Rather the smoothing of the raw topography, necessary to prevent coarse models from instigating grid-scale models, makes the ice sheet margin more gradual, causing the lower-elevation ablation zones to extend further away and outside the true ice sheet margin, resulting in the coarse cells in the ablation zone situated higher than the actual ice surface. This is another clue; the overextending of the ice sheet out over the ice margin means that these grid cells have multiple surface types within them. That is, It is these mixed ice/land/ocean grid cells tend to have the largest positive melt bias. It seems likely based on the transect that some of these largely biased coarse cells only have small fractions of ice, and so the state of the grid cell may be predominantly controlled by the land/ocean surface types.

Figure ?? shows the distribution of point-wise differences from LIVVkit observational database as violin plots. The IceBridge dataset is exclusively from the interior of the ice sheet and represents accumulation rates. The uniform 1° – 2° grids have similar median errors of about +35-50 mm.w.e, while the variable-resolution errors are noticeably smaller. The in-situ observations in the accumulation zone, shown in the middle plot looks very similar to the IceBridge errors, providing confidence that the variable-resolution grids are outperforming the uniform grids in the interior accumulation zone. The errors evaluated at in-situ ablation zone measurements are in tension with the RACMO results in Figure 10. They indicate that the uniform 1° – 2° grids perform similarly, and

478 that the *ARCTICGRIS* performs best, and an improvement over the *ARCTIC* grid.
 479 However, the in-situ ablation measurements are sparse in time and space, and so there
 480 is a large amount of uncertainty in extending these results to the entirety of the abla-
 481 tion zone.

482 The “k-transect” is perhaps the most well studied transect in Greenland, as it has
 483 been regularly monitored since the 1950s. The LIVVkit has compiled the k-transect ob-
 484 servations, shown in Figure ?? as elevation vs. SMB along the transect, with the model’s
 485 simulated transects shown as well. The in-situ observation points are nicely replicated
 486 by the *ARCTCIGRIS* run, whereas the *ARCTIC* grid is biased positive in the higher-
 487 elevations of the ablation zone. The *f09* grid is surprisingly competitive with the variable-
 488 resolution grids, capturing a realistic slope of the elevation-SMB curve, although it ex-
 489 hibits a similar positive bias as the *ARCTIC* grid. The elevation-SMB slopes of the uni-
 490 form spectral-element and *f19* grid are too shallow, in particular at the higher elevation
 491 regions of the transect.

492 Figure 13 shows the representation of the surface of the ice sheet along these tran-
 493 sects in the different grids, compared to the high resolution dataset used to generate CAM
 494 topography boundary conditions. The 1° – 2° grids are noticeably coarse, with only a
 495 handful of grid cells populating the transect. The *f09* grid is a bit of an exception –since
 496 the grid cells become very narrow in the meridional direction at high latitudes, a larger
 497 number of grid cells can populate the east-west transect, consistent with its skillful rep-
 498 resentation of the ablation zone.

499 What the authors refer to as the “b-transect” in northwest Greenland (Figure ??) is
 500 characterized by orographic precipitation, resulting in the accumulation zone extend-
 501 ing down to the ice margin. The variable resolution grids perform relatively well, with
 502 larger SMBs at lower elevations where the precipitation rates are highest, whereas the
 503 1° – 2° grids underestimate the SMB in these lower elevation regions. Only the vari-
 504 able resolution grids can capture the local reduction in SMB in the 1500-2000 m region.
 505 The skill of the variable-resolution grids is clearly related to the more accurate repre-
 506 sentation of the steepness of the transect, while also capturing the protrusion around 1500-
 507 2000 m that coincides with the local minimum in SMB (Figure 13).

508 To give an idea of what the ablation zones look like in the highest resolution *ARCTCIGRIS*
 509 grid, Figure ?? is a still from a visualization produced by the authors. It shows the daily
 510 mean surface mass balance during the height of the melt season in year 1981 of the sim-
 511 ulation. The ablation zone appears to be well resolved in the *ARCTICGRIS* grid. The
 512 full visualization is publicly available on youtube.com¹.

513 3.4 Precipitation extremes

514 Synoptic storms are tracked and analyzed using TempestExtremes (Ullrich et al.,
 515 2021). As the *ARCTIC* grid contains $\frac{1}{4}^{\circ}$ refinement north of about 45° latitude, the storm
 516 tracker is applied to this region for the *ARCTIC* and *ne30pg3* run to identify differences
 517 in storm characteristics due to horizontal resolution. Figure ?? shows the mean precip-
 518 itation rates averaged over all January storms identified by TempestExtremes. The iconic
 519 comma structure of the synoptic cyclones is simulated in *ne30pg3* and *ARCTIC* grids,
 520 with the magnitudes about the same in these two grids, with perhaps a marginal increase
 521 in precipitation rates in the storm center of the *ARCTIC* grid. For good measure, the
 522 *ne30pg3** run is also plotted, and looks more-or-less identical to the *ne30pg3* run.

523 As has been previously reported, horizontal resolution can have large impacts on
 524 extreme precipitation events. Figure 15 is a PDF of the precipitation rates associated

¹ https://www.youtube.com/watch?v=YwHgqDu75s8&t=4s&ab_channel=NCARVisLab

525 with synoptic storms, by month. The PDFs are constructed by sampling all the precipitation
 526 rates within 30° of the storm center, for each point on the storm track and for
 527 all storms. The PDFs are evaluated on an identical composite grid for all runs, and so
 528 storm statistics are not impacted by differences in output resolution. The *ARCTIC* run
 529 has larger extreme precipitation rates compared to *ne30pg3* in every month, but the in-
 530 crease is greatest in the summer months, which coincides with the most extreme events
 531 of the year. This is primarily due to an increase in resolution, and not the reduced physics
 532 times-step; the *ne30pg3** only marginally increases the precipitation rates compared with
 533 *ne30pg3*.

534 The extreme precipitation rates in the *ARCTIC* run are closer to the ERA5 re-
 535 analysis than in *ne30pg3* (Figure 15). It's difficult to know the extent that the extreme
 536 precipitation rates in ERA5 are constrained by data assimilation, or whether these pre-
 537 cipitation rates are due to using a similar $\frac{1}{4}^\circ$ model as the *ARCTIC* grid. However, it
 538 is well documented that $\frac{1}{4}^\circ$ models are more skillful at simulating extreme events (Bacmeister
 539 et al., 2013; O'Brien et al., 2016), and so this is an additional benefit of the variable-resolution
 540 grids.

541 4 Conclusions

542 Six grids from different dynamical cores in CESM2.2 are evaluated in an AMIP-
 543 style configuration for their performance over the Arctic and in simulating the Green-
 544 land Ice Sheet (GrIS) surface mass balance (SMB). The $1-2^\circ$ finite-volume grids have
 545 enhanced resolution over Polar regions due to the convergence of meridian lines, although
 546 a polar filter is employed to prevent features from forming at this higher resolution. Spectral-
 547 element grids comparable to the resolution of the finite-volume grids have an isotropic
 548 grid structure, meaning the grid resolution is similar over the entire domain. Two variable-
 549 resolution grids were developed and introduced into CESM2.2 as part of this work. They
 550 use the spectral-element dycore; the *ARCTIC* grid has $\frac{1}{4}^\circ$ refinement over the broader
 551 Arctic, whereas the *ARCTICGRIS* grid is identical except it has an $\frac{1}{8}^\circ$ patch of refine-
 552 ment over Greenland.

553 In general, the finite-volume grids have colder summer temperatures over the Arctic,
 554 and the spectral-element grids (incl. the variable-resolution grids) are warmer. The
 555 cloud biases in all the uniform resolution grids, whether finite-volume or spectral-elements,
 556 are similar, in general being too cloudy over Arctic land masses. The variable-resolution
 557 grids largely improve the cloud biases. It should be emphasized that our analysis is spe-
 558 cific to the Arctic summer due to its relevance to melt rates over GrIS; improved clouds
 559 in the Arctic should not be taken to mean that lower latitude regions have an improved
 560 cloud field as well.

561 At the regional level, a halo of negative cloud bias is found around the oceanic perime-
 562 ter of Greenland in all $1-2^\circ$ grids, and is absent in the variable-resolution grids. This
 563 halo bias coincides with a positive cloud bias over the interior of the ice sheet. This has
 564 been traced back to the inadequacy of the lower resolution grids to resolve the orographic
 565 precipitation process in Greenland. Synoptic systems moving into Greenland are not suf-
 566 ficiently lifted when encountering the steep ice margins due to overly smooth topogra-
 567 phy in the $1 - 2^\circ$ grids. As a result, moisture penetrates across the ice margin and
 568 dumps excess precipitation into the interior of the GrIS, instead of being concentrated
 569 closer to the coastal margins as indicated by observations. This results in a positive pre-
 570 cipitation and cloud bias in the ice sheet interior, and a halo of low cloud bias about the
 571 perimeter of Greenland. The agreement of different observational data products on this
 572 bias lends confidence in attributing the cause of the precipitation and cloud biases. The
 573 variable-resolution grids compare more favorably to the observations and indicate the
 574 orographic precipitation process in Greenland is largely resolved.

575 The primary source and sink terms of the SMB equation are integrated over the
 576 GrIS, and evaluated in the six grids. The uniform $1 - 2^\circ$ grids all have large positive
 577 accumulation biases owing to their inability to resolve the orographic precipitation pro-
 578 cess. The uniform spectral-element grids have larger accumulation biases, suggesting that
 579 the finite-volume grids are more skillful at resolving the precipitation processes due to
 580 their finer grid spacing over Greenland, despite the polar filter. The variable resolution
 581 grids have the most accurate accumulation rates of all the grids.

582 The primary mass sink term of the GrIS, ice/snow melt, expresses similar biases
 583 as the accumulation rates. The uniform resolution spectral-element grids melt too much,
 584 while the finite-volume grids have reduced biases. It's more difficult to attribute these
 585 biases to grid resolution alone; the finite-volume grids have colder summers that is con-
 586 sistent with their lower melt bias. However, the *ARCTICGRIS* grid has the warmest
 587 summer temperatures of all grids, yet it has reduced melting compared to the uniform
 588 resolution spectral-element grids. This suggests that grid resolution is responsible for a
 589 large fraction of the melt biases. That the melt process would be sensitive to grid res-
 590 olution is intuitive, since local elevation impacts on temperature and melting is largely
 591 handled by the land model, which does not have a pole problem because there is no hor-
 592 izontal dynamics. The larger number of grid cells in the ablation zone in the finite-volume
 593 grids seems to more accurately resolve the melt process relative to the uniform resolu-
 594 tion spectral-element grids, in which the ablation zone is made up of substantially fewer
 595 grid cells.

596 Acknowledgments

597 This material is based upon work supported by the National Center for Atmospheric Re-
 598 search (NCAR), which is a major facility sponsored by the NSF under Cooperative Agree-
 599 ment 1852977. Computing and data storage resources, including the Cheyenne super-
 600 computer (doi:10.5065/D6RX99HX), were provided by the Computational and Infor-
 601 mation Systems Laboratory (CISL) at NCAR.

602 The data presented in this manuscript is available at <https://github.com/adamrher/2020-arcticgrids>.

604 References

- 605 Bacmeister, J. T., Wehner, M. F., Neale, R. B., Gettelman, A., Hannay, C., Lau-
 606 ritzen, P. H., ... Truesdale, J. E. (2013). Exploratory high-resolution climate
 607 simulations using the community atmosphere model (cam). *J. Climate*, 27(9),
 608 3073–3099. doi: 10.1175/JCLI-D-13-00387.1
- 609 Beljaars, A., Brown, A., & Wood, N. (2004). A new parametrization of turbulent
 610 orographic form drag. *Quart. J. Roy. Meteor. Soc.*, 130(599), 1327–1347. doi:
 611 10.1256/qj.03.73
- 612 Bogenschutz, P. A., Gettelman, A., Morrison, H., Larson, V. E., Craig, C., & Scha-
 613 nen, D. P. (2013). Higher-order turbulence closure and its impact on climate
 614 simulations in the community atmosphere model. *Journal of Climate*, 26(23),
 615 9655–9676.
- 616 Braithwaite, R. J. (1984). Calculation of degree-days for glacier-climate research.
 617 *Zeitschrift für Gletscherkunde und Glazialgeologie*, 20(1984), 1–8.
- 618 Bromwich, D. H., Cassano, J. J., Klein, T., Heinemann, G., Hines, K. M., Steffen,
 619 K., & Box, J. E. (2001). Mesoscale modeling of katabatic winds over greenland
 620 with the polar mm5. *Monthly Weather Review*, 129(9), 2290–2309.
- 621 Calov, R., & Greve, R. (2005). A semi-analytical solution for the positive degree-day
 622 model with stochastic temperature variations. *Journal of Glaciology*, 51(172),
 623 173–175.
- 624 Canuto, C., Hussaini, M. Y., Quarteroni, A., & Zang, T. (2007). *Spectral methods*:

- 625 *Evolution to complex geometries and applications to fluid dynamics* (1st ed.).
 626 Springer.
- 627 Chepfer, H., Bony, S., Winker, D., Cesana, G., Dufresne, J., Minnis, P., ... Zeng, S.
 628 (2010). The gcm-oriented calipso cloud product (calipso-goccp). *Journal of
 629 Geophysical Research: Atmospheres*, *115*(D4).
- 630 Collins, W. D., Rasch, P. J., Boville, B. A., Hack, J. J., McCaa, J. R., Williamson,
 631 D. L., ... Zhang, M. (2006). The formulation and atmospheric simulation
 632 of the community atmosphere model version 3 (cam3). *Journal of Climate*,
 633 *19*(11), 2144–2161.
- 634 Copernicus, C. (2019). Era5 monthly averaged data on pressure levels from
 635 1979 to present. URL: <https://cds.climate.copernicus.eu>. doi: 10.24381/
 636 cds.6860a573
- 637 Craig, C., Bacmeister, J., Callaghan, P., Eaton, B., Gettelman, A., Goldhaber, S. N.,
 638 ... Vitt, F. M. (2021). *Cam6.3 user's guide* (Tech. Rep.). NCAR/TN-
 639 571+EDD. doi: 10.5065/Z953-ZC95
- 640 Danabasoglu, G., Lamarque, J.-F., Bacmeister, J., Bailey, D., DuVivier, A., Ed-
 641 wards, J., ... others (2020). The community earth system model ver-
 642 sion 2 (cesm2). *Journal of Advances in Modeling Earth Systems*, *12*(2),
 643 e2019MS001916.
- 644 Dennis, J. M., Edwards, J., Evans, K. J., Guba, O., Lauritzen, P. H., Mirin, A. A.,
 645 ... Worley, P. H. (2012). CAM-SE: A scalable spectral element dynamical
 646 core for the Community Atmosphere Model. *Int. J. High. Perform. C.*, *26*(1),
 647 74–89. Retrieved from <http://hpc.sagepub.com/content/26/1/74.abstract>
 648 doi: 10.1177/1094342011428142
- 649 Evans, K. J., Kennedy, J. H., Lu, D., Forrester, M. M., Price, S., Fyke, J., ... oth-
 650 ers (2019). Livykit 2.1: automated and extensible ice sheet model validation.
 651 *Geoscientific Model Development*, *12*(3), 1067–1086.
- 652 Gettelman, A., Morrison, H., Santos, S., Bogsenschutz, P., & Caldwell, P. (2015).
 653 Advanced two-moment bulk microphysics for global models. part ii: Global
 654 model solutions and aerosol–cloud interactions. *Journal of Climate*, *28*(3),
 655 1288–1307.
- 656 Golaz, J.-C., Larson, V. E., & Cotton, W. R. (2002). A pdf-based model for bound-
 657 ary layer clouds. part i: Method and model description. *Journal of the Atmo-
 658 spheric Sciences*, *59*(24), 3540–3551. doi: 10.1175/1520-0469(2002)059<3540:
 659 apbmfb>2.0.co;2
- 660 Guba, O., Taylor, M. A., Ullrich, P. A., Overfelt, J. R., & Levy, M. N. (2014). The
 661 spectral element method (sem) on variable-resolution grids: evaluating grid
 662 sensitivity and resolution-aware numerical viscosity. *Geosci. Model Dev.*, *7*(6),
 663 2803–2816. doi: 10.5194/gmd-7-2803-2014
- 664 Guo, Z., Wang, M., Qian, Y., Larson, V. E., Ghan, S., Ovchinnikov, M., ... Zhou,
 665 T. (2015). Parametric behaviors of clubb in simulations of low clouds in the c
 666 ommunity atmosphere model (cam). *Journal of Advances in Modeling Earth
 667 Systems*, *7*(3), 1005–1025.
- 668 Hansen, N., Simonsen, S. B., Boberg, F., Kittel, C., Orr, A., Souverijns, N., ... Mot-
 669 tram, R. (2022). Brief communication: Impact of common ice mask in surface
 670 mass balance estimates over the antarctic ice sheet. *The Cryosphere*, *16*(2),
 671 711–718.
- 672 Herrington, A., Lauritzen, P., Taylor, M. A., Goldhaber, S., Eaton, B. E., Bacmeis-
 673 ter, J., ... Ullrich, P. (2018). Physics-dynamics coupling with element-based
 674 high-order galerkin methods: quasi equal-area physics grid. *Mon. Wea. Rev.*,
 675 *47*, 69–84. doi: 10.1175/MWR-D-18-0136.1
- 676 Herrington, A., & Reed, K. (2018). An idealized test of the response of the commu-
 677 nity atmosphere model to near-grid-scale forcing across hydrostatic resolutions.
 678 *J. Adv. Model. Earth Syst.*, *10*(2), 560–575.
- 679 Herrington, A. R., Lauritzen, P. H., Reed, K. A., Goldhaber, S., & Eaton, B. E.

- (2019). Exploring a lower resolution physics grid in cam-se-cslam. *Journal of Advances in Modeling Earth Systems*, 11.
- Herrington, A. R., & Reed, K. A. (2020). On resolution sensitivity in the community atmosphere model. *Quarterly Journal of the Royal Meteorological Society*, 146(733), 3789–3807.
- Hurrell, J. W., Hack, J. J., Shea, D., Caron, J. M., & Rosinski, J. (2008). A new sea surface temperature and sea ice boundary dataset for the community atmosphere model. *Journal of Climate*, 21(19), 5145–5153.
- Jablonowski, C., & Williamson, D. L. (2006). A baroclinic instability test case for atmospheric model dynamical cores. *Q. J. R. Meteorol. Soc.*, 132, 2943–2975.
- Jablonowski, C., & Williamson, D. L. (2011). The pros and cons of diffusion, filters and fixers in atmospheric general circulation models., in: P.H. Lauritzen, R.D. Nair, C. Jablonowski, M. Taylor (Eds.), Numerical techniques for global atmospheric models. *Lecture Notes in Computational Science and Engineering*, Springer, 80.
- Lauritzen, P. H., Bacmeister, J. T., Callaghan, P. F., & Taylor, M. A. (2015). Near global model topography generation software for unstructured grids. *Geoscientific Model Development Discussions*, 8(6), 4623–4651. doi: 10.5194/gmdd-8-4623-2015
- Lauritzen, P. H., Mirin, A., Truesdale, J., Raeder, K., Anderson, J., Bacmeister, J., & Neale, R. B. (2011). Implementation of new diffusion/filtering operators in the CAM-FV dynamical core. *Int. J. High Perform. Comput. Appl.*. doi: 10.1177/10943432011410088
- Lauritzen, P. H., Nair, R., Herrington, A., Callaghan, P., Goldhaber, S., Dennis, J., ... Dubos, T. (2018). NCAR CESM2.0 release of CAM-SE: A reformulation of the spectral-element dynamical core in dry-mass vertical coordinates with comprehensive treatment of condensates and energy. *J. Adv. Model. Earth Syst.*. doi: 10.1029/2017MS001257
- Lauritzen, P. H., Taylor, M. A., Overfelt, J., Ullrich, P. A., Nair, R. D., Goldhaber, S., & Kelly, R. (2017). CAM-SE-CSLM: Consistent coupling of a conservative semi-lagrangian finite-volume method with spectral element dynamics. *Mon. Wea. Rev.*, 145(3), 833–855. doi: 10.1175/MWR-D-16-0258.1
- Lawrence, D. M., Fisher, R. A., Koven, C. D., Oleson, K. W., Swenson, S. C., Bonan, G., ... others (2019). The community land model version 5: Description of new features, benchmarking, and impact of forcing uncertainty. *Journal of Advances in Modeling Earth Systems*, 11(12), 4245–4287.
- Lin, S.-J. (2004). A 'vertically Lagrangian' finite-volume dynamical core for global models. *Mon. Wea. Rev.*, 132, 2293–2307.
- Lin, S.-J., & Rood, R. B. (1997). An explicit flux-form semi-Lagrangian shallow-water model on the sphere. *Q.J.R.Meteorol.Soc.*, 123, 2477–2498.
- Lipscomb, W. H., Fyke, J. G., Vizcaíno, M., Sacks, W. J., Wolfe, J., Vertenstein, M., ... Lawrence, D. M. (2013). Implementation and initial evaluation of the glimmer community ice sheet model in the community earth system model. *Journal of Climate*, 26(19), 7352–7371.
- Loeb, N. G., Doelling, D. R., Wang, H., Su, W., Nguyen, C., Corbett, J. G., ... Kato, S. (2018). Clouds and the earth's radiant energy system (ceres) energy balanced and filled (ebaf) top-of-atmosphere (toa) edition-4.0 data product. *Journal of Climate*, 31(2), 895–918.
- Lofverstrom, M., Fyke, J. G., Thayer-Calder, K., Muntjewerf, L., Vizcaino, M., Sacks, W. J., ... Bradley, S. L. (2020). An efficient ice sheet/earth system model spin-up procedure for cesm2-cism2: Description, evaluation, and broader applicability. *Journal of Advances in Modeling Earth Systems*, 12(8), e2019MS001984.
- Neale, R. B., Richter, J. H., & Jochum, M. (2008). The impact of convection on ENSO: From a delayed oscillator to a series of events. *J. Climate*, 21, 5904–

- 735 5924.
- 736 Noël, B., Van De Berg, W., Van Meijgaard, E., Kuipers Munneke, P., Van De Wal,
 737 R., & Van Den Broeke, M. (2015). Evaluation of the updated regional climate
 738 model racmo2. 3: summer snowfall impact on the greenland ice sheet. *The*
 739 *Cryosphere*, *9*(5), 1831–1844.
- 740 Noël, B., van de Berg, W. J., Lhermitte, S., & van den Broeke, M. R. (2019). Rapid
 741 ablation zone expansion amplifies north greenland mass loss. *Science advances*,
 742 *5*(9), eaaw0123.
- 743 O'Brien, T. A., Collins, W. D., Kashinath, K., Rübel, O., Byna, S., Gu, J., ...
 744 Ullrich, P. A. (2016). Resolution dependence of precipitation statistical
 745 fidelity in hindcast simulations. *J. Adv. Model. Earth Syst.*, *8*(2), 976–
 746 990. Retrieved from <http://dx.doi.org/10.1002/2016ms000671> doi:
 747 10.1002/2016ms000671
- 748 Ohmura, A. (2001). Physical basis for the temperature-based melt-index method.
 749 *Journal of applied Meteorology*, *40*(4), 753–761.
- 750 Pollard, D. (2010). A retrospective look at coupled ice sheet–climate modeling. *Cli-*
 751 *matic Change*, *100*(1), 173–194.
- 752 Pope, V., & Stratton, R. (2002). The processes governing horizontal resolution sensi-
 753 tivity in a climate model. *Climate Dynamics*, *19*(3-4), 211–236.
- 754 Putman, W. M., & Lin, S.-J. (2007). Finite-volume transport on various cubed-
 755 sphere grids. *J. Comput. Phys.*, *227*(1), 55–78.
- 756 Reeh, N. (1991). Parameterization of melt rate and surface temperature in the
 757 greenland ice sheet. *Polarforschung*, *59*(3), 113–128.
- 758 Richter, J. H., Sassi, F., & Garcia, R. R. (2010). Toward a physically based gravity
 759 wave source parameterization in a general circulation model. *J. Atmos. Sci.*,
 760 *67*, 136–156. doi: dx.doi.org/10.1175/2009JAS3112.1
- 761 Rignot, E., & Mouginot, J. (2012). Ice flow in greenland for the international polar
 762 year 2008–2009. *Geophysical Research Letters*, *39*(11).
- 763 Roeckner, E., Brokopf, R., Esch, M., Giorgetta, M., Hagemann, S., Kornblueh, L.,
 764 ... Schulzweida, U. (2006). Sensitivity of simulated climate to horizontal
 765 and vertical resolution in the echam5 atmosphere model. *Journal of Climate*,
 766 *19*(16), 3771–3791.
- 767 Sellevold, R., Van Kampenhout, L., Lenaerts, J., Noël, B., Lipscomb, W. H., &
 768 Vizcaino, M. (2019). Surface mass balance downscaling through elevation
 769 classes in an earth system model: Application to the greenland ice sheet. *The*
 770 *Cryosphere*, *13*(12), 3193–3208.
- 771 Smirnova, J., & Golubkin, P. (2017). Comparing polar lows in atmospheric reanal-
 772 yses: Arctic system reanalysis versus era-interim. *Monthly Weather Review*,
 773 *145*(6), 2375–2383.
- 774 Stocker, T. (2014). *Climate change 2013: the physical science basis: Working group*
 775 *i contribution to the fifth assessment report of the intergovernmental panel on*
 776 *climate change*. Cambridge university press.
- 777 Suarez, M. J., & Takacs, L. L. (1995). Volume 5 documentation of the aries/geos dy-
 778 namical core: Version 2.
- 779 Taylor, M. A., & Fournier, A. (2010). A compatible and conservative spectral el-
 780 ement method on unstructured grids. *J. Comput. Phys.*, *229*(17), 5879 - 5895.
 781 doi: 10.1016/j.jcp.2010.04.008
- 782 Taylor, M. A., Tribbia, J., & Iskandarani, M. (1997). The spectral element method
 783 for the shallow water equations on the sphere. *J. Comput. Phys.*, *130*, 92-108.
- 784 Team, E. J. S., Balaji, V., Boville, B., Collins, N., Craig, T., Cruz, C., ... others
 785 (2021). *Esmf user guide* (Tech. Rep.).
- 786 Ullrich, P. A., & Taylor, M. A. (2015). Arbitrary-order conservative and consis-
 787 tent remapping and a theory of linear maps: Part i. *Monthly Weather Review*,
 788 *143*(6), 2419–2440.
- 789 Ullrich, P. A., Zarzycki, C. M., McClenney, E. E., Pinheiro, M. C., Stansfield, A. M.,

- 790 & Reed, K. A. (2021). Tempestextremes v2. 1: a community framework for
791 feature detection, tracking and analysis in large datasets. *Geoscientific Model*
792 *Development Discussions*, 1–37.
- 793 van Kampenhout, L., Lenaerts, J. T., Lipscomb, W. H., Lhermitte, S., Noël, B.,
794 Vizcaíno, M., ... van den Broeke, M. R. (2020). Present-day greenland ice
795 sheet climate and surface mass balance in cesm2. *Journal of Geophysical*
796 *Research: Earth Surface*, 125(2).
- 797 van Kampenhout, L., Rhoades, A. M., Herrington, A. R., Zarzycki, C. M., Lenaerts,
798 J. T. M., Sacks, W. J., & van den Broeke, M. R. (2018). Regional grid refine-
799 ment in an earth system model: Impacts on the simulated greenland surface
800 mass balance. *The Cryosphere Discuss..* doi: 10.5194/tc-2018-257
- 801 Williamson, D. (2007). The evolution of dynamical cores for global atmospheric
802 models. *J. Meteor. Soc. Japan*, 85, 241-269.
- 803 Williamson, D. L. (2008). Convergence of aqua-planet simulations with increas-
804 ing resolution in the community atmospheric model, version 3. *Tellus A*, 60(5),
805 848–862. doi: 10.1111/j.1600-0870.2008.00339.x
- 806 Zhang, G., & McFarlane, N. (1995). Sensitivity of climate simulations to the pa-
807 rameterization of cumulus convection in the canadian climate centre general
808 circulation model. *Atmosphere-ocean*, 33(3), 407-446.

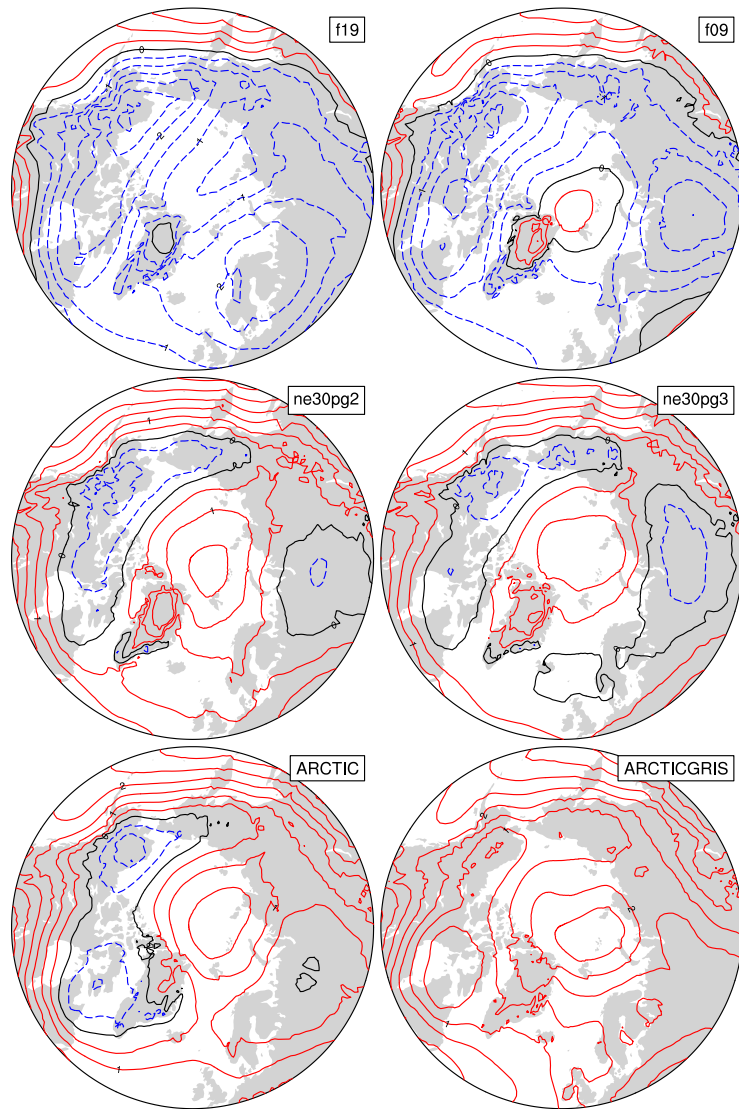


Figure 6. 1979-1998 lower troposphere, northern hemisphere summer virtual temperature biases, computed as the difference from ERA5. Lower troposphere layer mean virtual temperature is derived from the 1000 hPa - 500h Pa geopotential thickness, using the hypsometric equation. ERA5 is very high-resolution at high-latitudes owing to the use of a $\frac{1}{4}^{\circ}$ latitude-longitude grid, and so all model differences are computed after mapping ERA5 to their respective model grids.

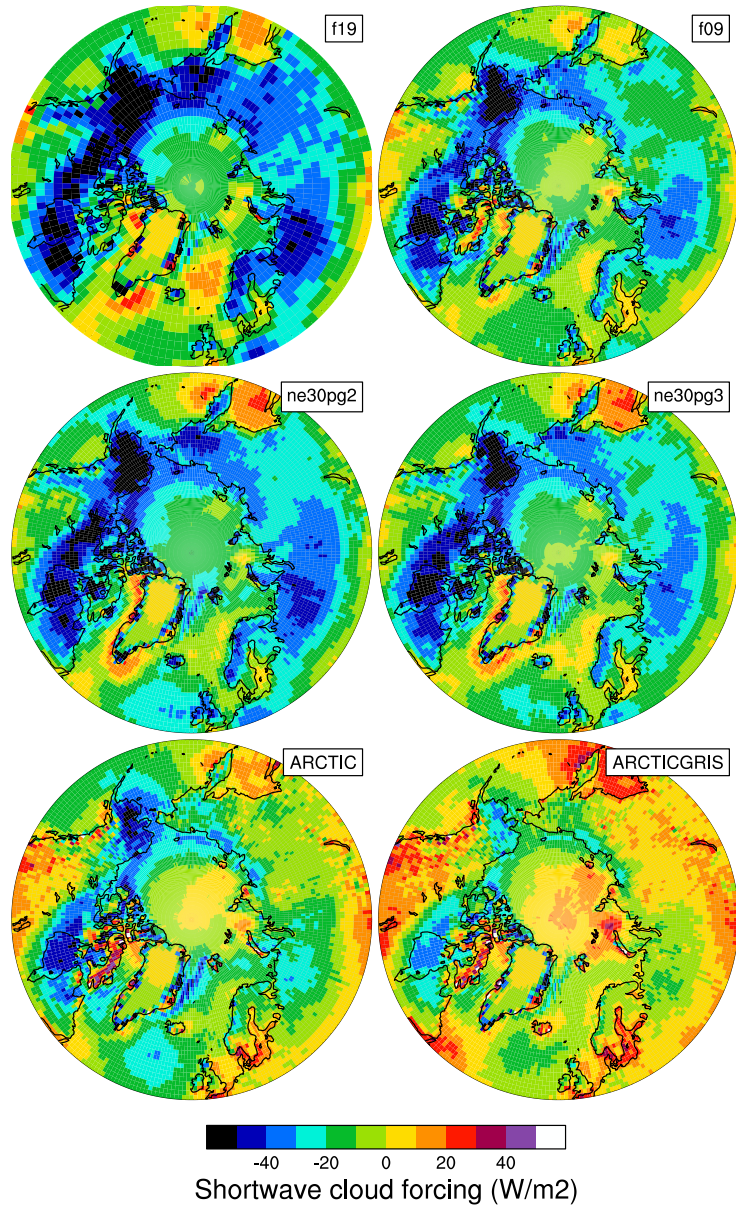


Figure 7. 1979-1998 northern hemisphere summer shortwave cloud forcing bias, relative to the CERES-EBAF gridded dataset. Differences are computed after mapping all model output to the 1° CERES-EBAF grid.

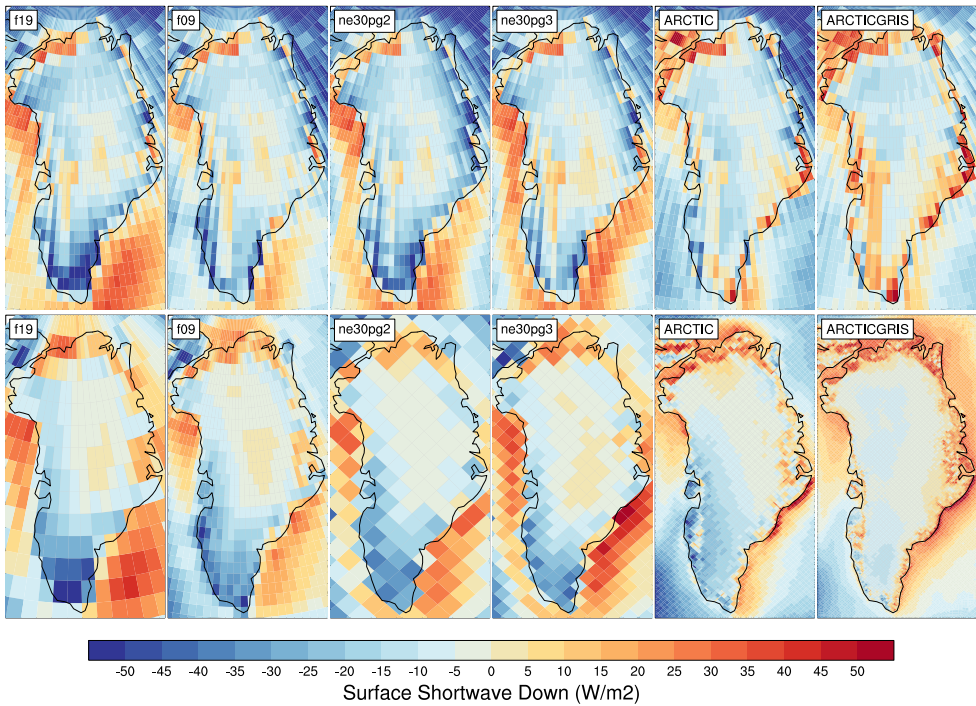


Figure 8. 1979-1998 northern hemisphere summer, incident shortwave radiation bias, computed as the difference (top) from CERES-EBAF, and (bottom) RACMO2.3p2 dataset. The differences in the top panel are found by mapping the model output to the 1° CERES-EBAF grid, and differences on the bottom panel are computed after mapping the RACMO2.3p2 dataset to the individual model grids. Note that the averaging period for the CERES-EBAF panels, 2003-2020, is different from the averaging period for the model results.

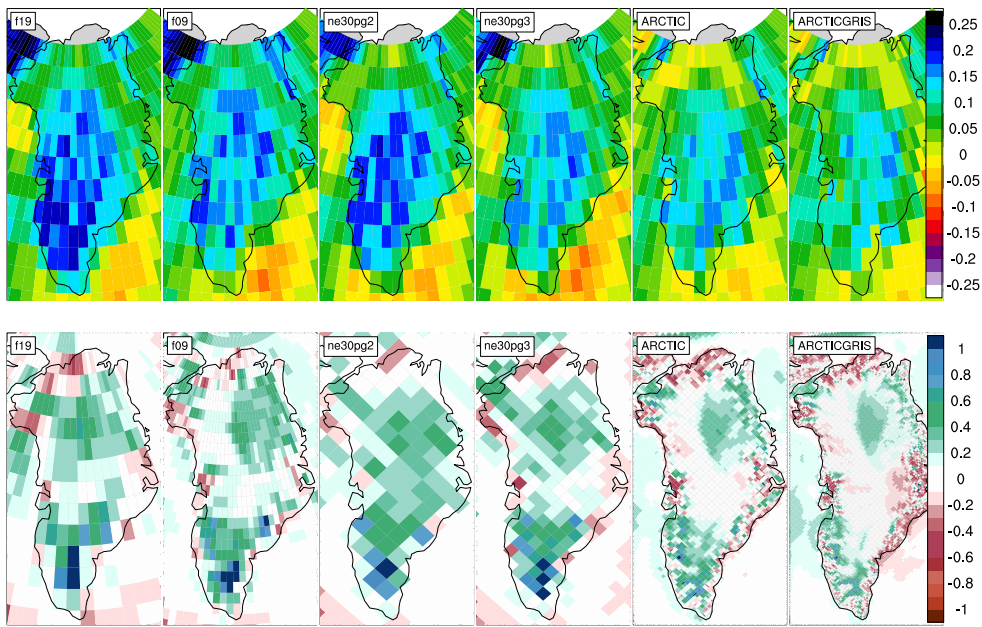


Figure 9. 1979-1998 northern hemisphere summer (top) total cloud fraction bias, relative to the CALIPSO-GOCCP dataset, and (bottom) precipitation rate bias, relative to the RACMO2.3p2 dataset. The CALIPSO-GOCCP differences are computed after mapping all model output to the 1° grid, whereas the RACMO differences are computed after mapping the RACMO dataset to the individual model grids. Note that the averaging period for the CALIPSO-GOCCP panels, 2006-2017, is different than the model averaging period.

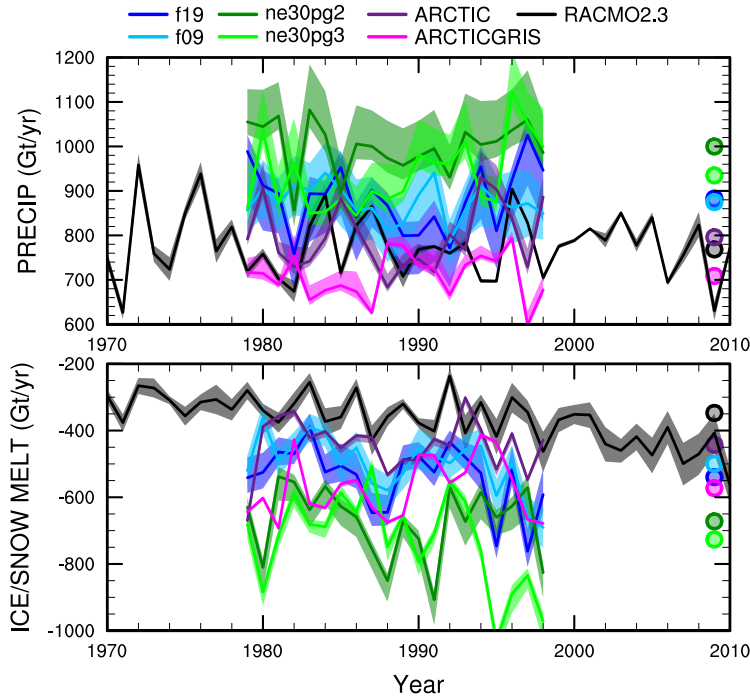


Figure 10. Time-series of annual (solid+liquid) precipitation (top) and annual runoff (bottom) integrated over the Greenland Ice Sheet for all six simulations and compared to RACMO3.2. The raw fields are mapped to two target low resolution grids, f19 & ne30pg2, and using two different remapping methods, conservative ESMF and high order TempestRemap. The remapped values are then integrated over the ice mask of the target grid. This gives four time-series for each simulation (three for f19 & ne30pg2), with the mean value given by the solid line and shading spanning the extent of the remapped solutions.

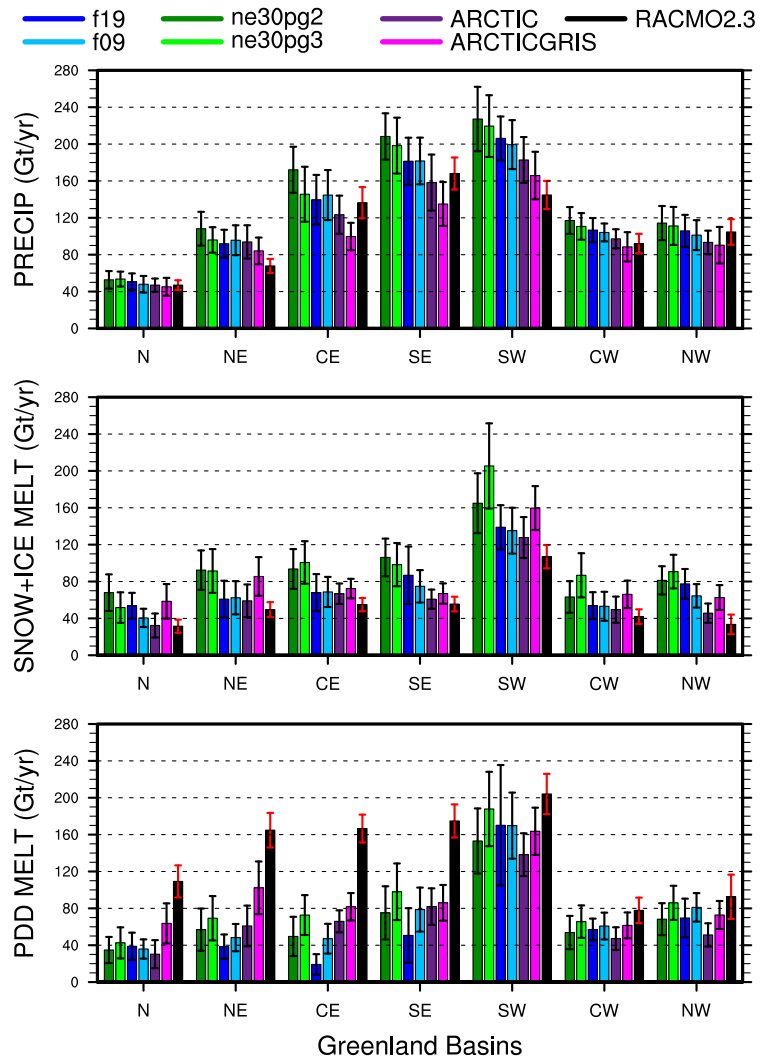


Figure 11.

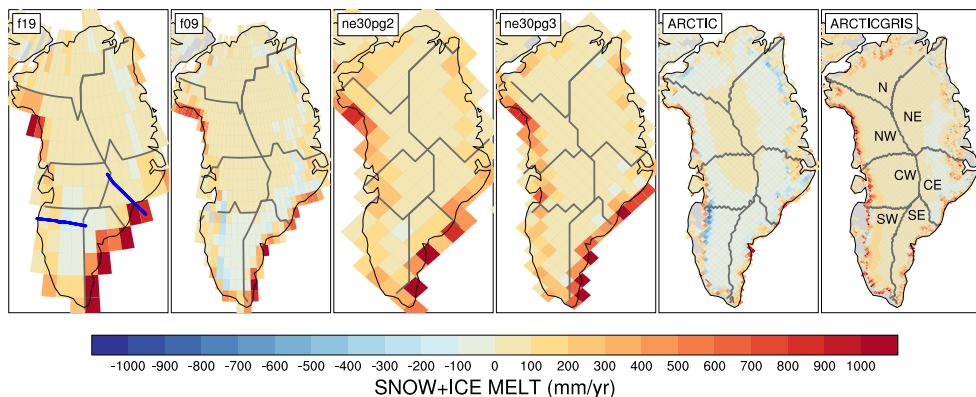


Figure 12.

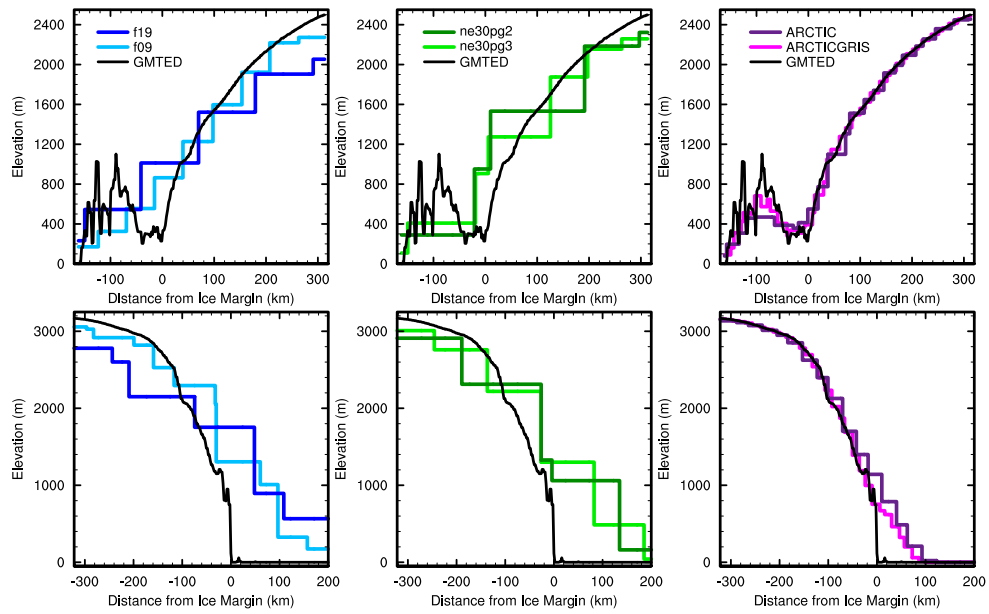


Figure 13. .

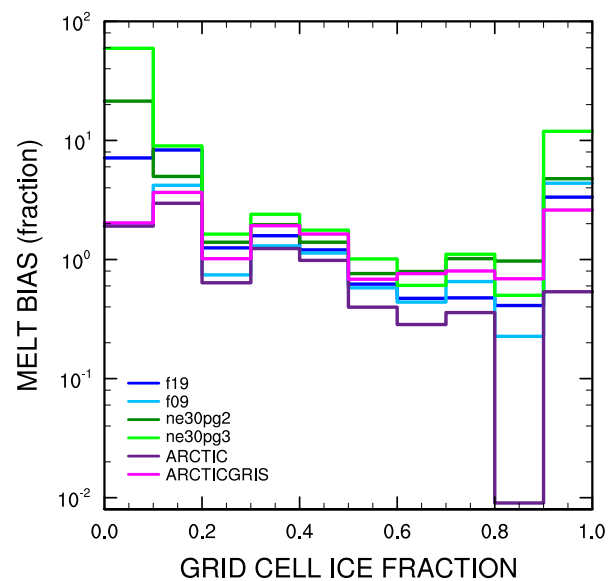


Figure 14. .

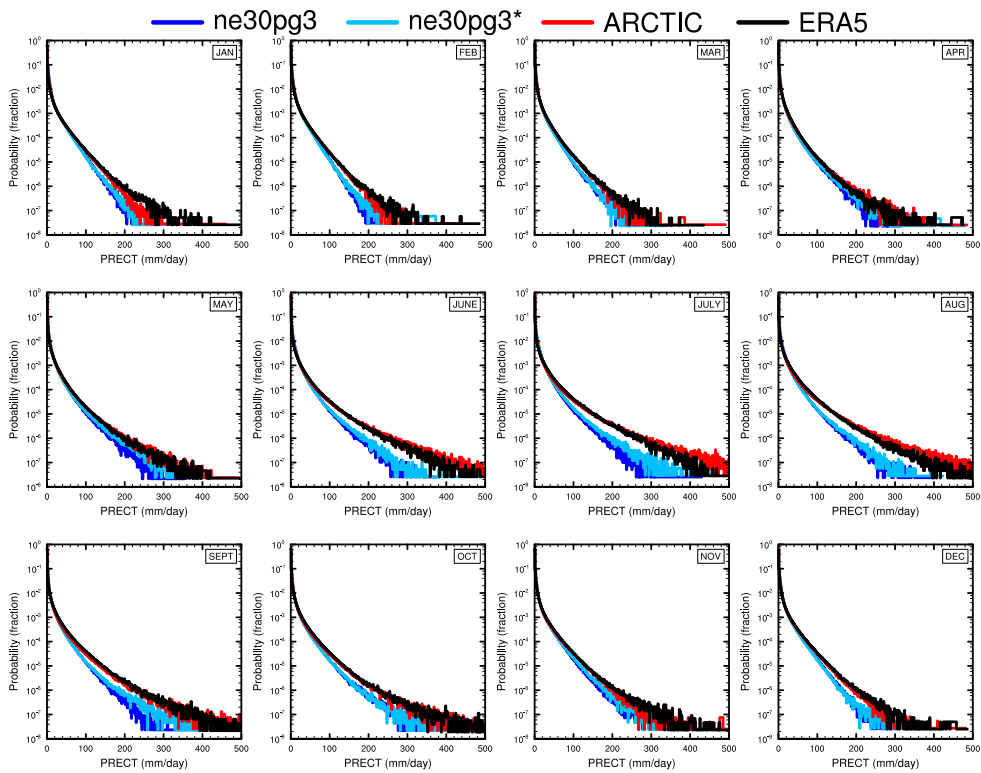


Figure 15.